Assessment of optical phonons in BeTe, BexZn1-xTe, p-BeTe epilayers and BeTe/ZnTe/GaAs (001) superlattices

Citation: Applied Physics A. 2022 Jul 21;128(8):702

As Published: https://doi.org/10.1007/s00339-022-05819-z

Publisher: Springer Berlin Heidelberg

Persistent URL: https://hdl.handle.net/1721.1/143951

Version: Author's final manuscript: final author's manuscript post peer review, without publisher's formatting or copy editing

Assessment of optical phonons in BeTe, BexZn1-xTe, p-BeTe epilayers and BeTe/ZnTe/GaAs (001) superlattices

Assessment of optical phonons in BeTe, $Be_xZn_{1-x}Te$, p-BeTe epilayers and BeTe/ZnTe/GaAs (001) superlattices

Devki N. Talwar [a,b] and P. Becla [c]

[a] *Department of Physics, University of North Florida, 1 UNF Drive, Jacksonville, Florida 32224-7699, USA, and*

[b] *Department of Physics, Indiana University of Pennsylvania, 975 Oakland Avenue, 56 Weyandt Hall, Indiana, Pennsylvania 15705-1087, USA,*

[c] *Department of Materials Science and Engineering, Massachusetts Institute of Technology, Cambridge, Massachusetts 02139, USA*

Abstract

Comprehensive simulations for the polarization dependent far-infrared (FIR) reflectance and transmission spectra are reported to assess the longitudinal optical (ω_{LO}) and transverse optical (ω_{TO}) phonons in binary BeTe (ZnTe)/GaAs (001), ternary alloy $Be_xZn_{1-x}Te$/GaAs (001) epilayers and BeTe/ZnTe/GaAs (001) superlattices. The Kramers-Krönig analyses are performed to achieve the optical constants of bulk materials for constructing their frequency dependent dielectric functions. Both s-$[T_s(\omega)/R_s(\omega)]$ and p-$[T_p(\omega)/R_p(\omega)]$ polarized spectral calculations are attained at an oblique incidence [i.e., Berreman effect (BE)] by using a three-phase model in a multilayer optics approach. For perfect thin epilayers, the BE method has offered an unambiguous appraisal of ω_{LO} and ω_{TO} phonons in the p-polarized $[T_p(\omega)/R_p(\omega)]$ FIR spectra, while in the p-doped BeTe epilayer it justified the LO-plasmon (ω^+_{LOPL}) coupled modes to be longitudinal in character. Careful assessment of the ω^+_{LOPL} by FIR spectroscopy offers an alternative, elegant and effective method, complementary to Raman scattering spectroscopy for estimating the free-carrier charge density η in technologically important doped semiconductor epilayers.

Key words: Berreman effect; Reflectance and transmission at oblique incidence; Multi-layer optics approach; LO-plasmon coupled modes

Corresponding author: Devki N. Talwar e-mail: d.talwar@unf.edu

1 Introduction

In recent years, the novel zinc-blende (zb) wide band gap $Be_xZn_{1-x}Te$ (BZT) alloys have gained considerable attention for many device applications in the optoelectronics [1-8]. The advantage of exploiting BZT materials is to control their basic physical properties in the entire composition range. The conventional zb ZnTe (2.26 eV) is a direct band gap E_g material and BeTe (2.8 eV) has an indirect band gap. Alloying these two compounds leads to a direct-indirect band gap crossover at a certain Be composition, x. While such a transition from the direct to indirect E_g is still unknown, the experimental evidence has suggested, however, that it occurs [1] at about x ~ 0.28. Molecular beam epitaxy (MBE) technique has been successfully employed to grow high quality (a) BZT ternary alloys on either GaAs and/or InP substrates [4-7], and (b) prepare p-type BZT samples [5-6] by incorporating nitrogen (N) to achieve charge carrier concentration η as high as ~ 4.8 x 10^{18} cm^{-3}. The photoluminescence (PL) measurements [3] on N-doped BZT have confirmed the p-type doping [5] in a wide visible-energy range. The use of p-BZT films has been established as an active layer and/or p-cladding layer for designing laser diodes (LDs) and light-emitting diode (LED) structures [5-8]. Several recently fabricated current injected LDs operating at 560 nm wavelength are successfully integrated in the optical recording, communications, as well as ultrahigh speed microwave transistors for wireless networks, cellular phones, and biological sensors, etc. [5-9]. Although III-N based (GaInN, AlInGaN) alloys and heterostructures [i.e., multi-quantum wells (MQWs), superlattices (SLs)] have also been employed to design the blue-green LEDs and LDs, however, major factors for acquiring lasing emission between 450 nm to 570 nm wavelength to achieve optimal device performances are not fully materialized [10-11]. Serious issues related to the efficiency of III-N based LEDs and requiring a high threshold current in the functioning of LDs are demanding major modifications.

As the veracity of using p-doped BZT alloys, BZT/ZnTe MQWs and BeTe/ZnTe SLs is intensified for designing the optoelectronic device structures in commercial applications [5-9], so does the obligations for scientists and engineers to comprehend their response to optical excitations in the far infrared (FIR) region for extracting basic characteristics [2-4]. Many key traits involved in the operations of optoelectronic devices are contingent on the materials longitudinal-optical (ω_{LO}), transverse-optical (ω_{TO}) phonons, charge carrier concentration η, as well as its distribution in both the active region and/or passive parts as waveguide claddings. Determining such attributes

experimentally in a nondestructive manner is crucial for improving the efficiency of device fabrication process. Except for ZnTe, where the complete phonon dispersions ($\omega_j(\vec{q})$) are available by inelastic neutron scattering (INS) experiments, [12] in the epitaxially grown BeTe, however, such measurements are not possible simply because the films are too lean to obtain measurable signals by resolving phonons lying close in frequency. Despite the importance of $Be_xZn_{1-x}Te$ alloys and BeTe/ZnTe SLs in optoelectronics, their phonon characteristics have not been fully explored. For comprehending the optical phonons in $Be_xZn_{1-x}Te$ alloys the only systematic study using Raman scattering spectroscopy (RSS) is by Pagès *et al.* [13]. In this investigation, the authors used MBE grown BZT samples of different composition ($0 \leq x \leq 0.525$) and thickness d ($\equiv 0.56$ μm to 1.62 μm). Measurements are performed in the backscattering geometry with a 647.1 nm radiation using Kr^+ laser beam along the growth- [001] as well as [110] edge-crystal axis. It is to be noted that in the conventional [001] direction, the ω_{LO} modes are allowed in the backscattering geometry while ω_{TO} phonons are forbidden by the selection rules [13]. In the [110] axis, however, the situation is reversed allowing the observation of ω_{TO} modes. For the ternary $Be_xZn_{1-x}Te$ alloys the observed composition dependent optical phonons by Raman scattering spectroscopy has confirmed a two-mode behavior [13], like many other conventional II-VI ($Cd_xZn_{1-x}Te$ and $Cd_xMg_{1-x}Te$) semiconductors [14-17]. Besides RSS [13], Mandal *et al.* [15] have also assessed the BeTe-related (ω_{LO}, ω_{TO}) modes in $Be_xZn_{1-x}Te$ ($0 \leq x \leq 0.378$) alloys by fitting the dielectric function ($\tilde{\varepsilon}(\omega)$) from the spectroscopic ellipsometry (SE) data. In doped BeTe (ZnTe) semiconductors, as the ω_{LO}, ω_{TO} modes and light absorption by charge carriers η dominate in the FIR dielectric function $\tilde{\varepsilon}(\omega)$, their precise knowledge is imperative for offering both the lattice phonons as well as carrier concentration in n- and/or p-type materials [2-4].

Complementary to Raman scattering [13], the FIR spectroscopy [16] is an equally powerful technique. In bulk polar materials, the conventional FIR studies are generally performed at near-normal incidence θ_i (= 0) for extracting ω_{TO} phonons. However, in ultrathin epifilms, the polarized transmission measurements at oblique incidence angle θ_i ($\neq 0$) (the Berreman effect (BE)) [17] are considered not only valuable but also compatible and superior to Raman scattering for perceiving both the ω_{LO} and ω_{TO} modes. This is simply because the ω_{TO} modes in the RSS near backscattering geometry [13] are either forbidden or appear weak and difficult to identify amidst disorder induced phonon continuum. In thin films, the p-polarized FIR transmission studies have been successfully

employed in recent years for assessing not only the optical (ω_{LO}, ω_{TO}) phonons of different perfect materials but also identifying the LO–phonon-plasmon ($\omega^{\pm}_{LOPL}$) coupled modes to estimate the charge carrier concentration η in n- and/or p-doped samples [18]. Such experimental studies have not been performed either on ultrathin BZT/GaAs (001) epilayers or N-doped BeTe samples.

The purpose of this paper is to report the results of a comprehensive study (cf. Sec. 2) by simulating the FIR reflectivity R(ω) and transmission T(ω) spectrum at near normal and oblique incidence for both the undoped and doped $Be_xZn_{1-x}Te$/GaAs (001) epilayers as well as BeTe/ZnTe/ GaAs (001) SLs (cf. Sec. 2.1 – 2.2). For bulk materials the appropriate dielectric dispersions are meticulously accomplished by using the Kramers-Krönig analyses to obtain the frequency dependent dielectric functions $\tilde{\varepsilon}(\omega)$. Least square fit to the reflectivity spectra [21-25] of bulk ZnTe, BeTe, $Be_{0.5}Zn_{0.5}Te$, and GaAs materials are achieved by exploiting the CERN library MINUIT program based on Metropolis algorithm. The resulting standard deviation σ has been achieved $\leq 5 \times 10^{-3}$ in all the fits of reflectivity spectra to accomplish the necessary phonon mode parameters (see: Table 1). In the framework of a three-phase model (cf. Sec. 3) and using a multi-layer optics methodology [19-20] we have systematically performed calculations of the s- and p-polarized reflectance [$R_{s,p}(\omega)$] and transmission [$T_{s,p}(\omega)$] spectra at oblique incidence (θ_i) by considering apposite Fresnel coefficients. The results of binary BeTe (ZnTe)/GaAs (001) and ternary alloy $Be_{0.5}Zn_{0.5}Te$/GaAs (001) epifilms as well as BeTe/ZnTe/GaAs (001) SLs (cf. Secs. 3.1 – 3.3) are accurately achieved by appropriately including the incident angle θ_i, alloy composition x, film thicknesses and SL period d ($\equiv d_{AB} + d_{AC}$). Our simulations have revealed that at small θ_i, the BE [17] provides an unambiguous assessment of the ω_{LO}, ω_{TO} phonons in binary, ternary alloys as well as SLs. The BeTe- (ZnTe-) type ω_{LO1}, ω_{TO1} (ω_{LO2}, ω_{TO2}) phonons acquired for the $Be_{0.5}Zn_{0.5}Te$ alloy (cf. Sec. 3.2.3) follow the x-dependent results of the two-mode behavior (cf. Sec. 3.4) for $Be_xZn_{1-x}Te$ alloys derived from a traditional modified-random-element-iso-displacement (MREI) model [13]. Extending this approach to N-doped BZT/GaAs epifilms has convincingly corroborated that the BE calculations of reflectivity/transmission are equally persuasive for distinguishing the ω^{+}_{LOPL} modes and extracting (cf. Sec. 3.3) the charge carrier concentration η. Theoretical results of optical phonons (ω_{LO}, ω_{TO}), ω^{+}_{LOPL} modes and η are compared/contrasted favorably well against the existing Raman scattering [13], INS [12], Hall and PL measurements [5] with concluding remarks presented in Sec. 4.

2. Theoretical background

There exist two types of theoretical methods for assessing the structural and lattice dynamical properties of perfect/imperfect semiconductors. These are: (a) the *microscopic* methods [26-38] which start with ionic potentials screened by electron gas for gaining the optical, electronic, and phonon traits, and (b) the *macroscopic* techniques, which employ phenomenological models [39–49] to simulate phonon and impurity-induced vibrational characteristics. In the former techniques, the interatomic forces of the perfect/imperfect materials are usually evaluated using self-consistent density functional theory (SC-DFT) [26–38] to comprehend the structural, optical, and phonon properties by employing an ABINIT software package. One must note that the SC-DFT methods are computationally demanding for semiconductor materials to study the defect vibrational modes of isoelectronic impurities and are much more cumbersome for non-isoelectronic (i.e., charged) defects [29]. The first-principles methods have offered not only accurate phonon properties of alloy semiconductors [26-38] but also facilitated assessing FIR reflectivity and Raman intensity profiles of perfect/imperfect GaN/AlN SLs [31-32]. As compared to the *ab initio* techniques, the benefits of using *macroscopic* methods for investigating the lattice dynamics of perfect/imperfect [39-49] semiconductors are quite discernable. Here we have adopted a macroscopic methodology of multilayer optics (cf. Secs. 2.1 – 2.5) for simulating the FIR reflectivity/transmission spectra of bulk binary (BeTe, ZnTe, BeZnTe, GaAs) materials, thin MBE grown ternary alloy epilayers Be(Zn)Te/GaAs (001) and BeTe/(ZnTe/GaAs (001) SLs. Theoretical results are compared/ contrasted with the existing experimental and theoretical (cf. Sec. 3) data.

2.1 Reflectivity and transmission of binary and ternary alloys

The infrared radiations through polar materials can couple strongly to their optical modes. The ω_{TO} and ω_{LO} phonons define a region of negative permittivity and the center of a section of high loss, is called the Reststrahlen band region.

To simulate the FIR reflectance and transmission spectra of bulk binary and ternary alloys, the physical process involving interactions between the electromagnetic (EM) radiation and materials can be articulated in terms of the complex refractive index $\tilde{n}(\omega)$ via their dielectric functions $\tilde{\varepsilon}(\omega)$ [$\tilde{n}(\omega) = \sqrt{\tilde{\varepsilon}(\omega)}$]. In zb semiconductors two main processes contribute to $\tilde{\varepsilon}(\omega)$: (a) the free-charge carrier effect in doped materials caused by electrons and/or holes, and (b) the lattice effect

from the optical phonons. To simplify the FIR reflectivity calculations, multi-phonon absorption method is not considered here. Instead, we have adopted a classical form of $\tilde{\varepsilon}(\omega)$ for the doped binary materials by using the Drude-Lorentz approach [16]:

$$\tilde{\varepsilon}(\omega) = \varepsilon_\infty \left[1 - \frac{\omega_P^2}{\omega^2 + i\omega\gamma}\right] + \frac{(\varepsilon_o - \varepsilon_\infty)\omega_{TO}^2}{\omega_{TO}^2 - \omega^2 - i\omega\Gamma} = \varepsilon_\infty \left[1 - \frac{\omega_P^2}{\omega^2 + i\omega\gamma}\right] + \frac{S\omega_{TO}^2}{\omega_{TO}^2 - \omega^2 - i\omega\Gamma} . \quad (1)$$

In Eq. (1), the first term on the right hand side describes the interaction between the charge carriers and EM wave of frequency ω; $\gamma(=\frac{1}{\tau})$ is the free carrier damping constant with relaxation time of τ; $\omega_P \left\{\equiv \left[\frac{4\pi\eta e^2}{m^*\varepsilon_\infty}\right]^{1/2}\right\}$ is the plasma frequency of free carrier concentration η with an effective mass m^*, and e is the magnitude of electron charge. The second term in Eq. (1) covers the Reststrahlen region describing the interaction of EM radiation with optical phonons, where ε_o and ε_∞ are, respectively the static and high-frequency dielectric constants. The term $S(\equiv (\varepsilon_o - \varepsilon_\infty)$ or $\equiv \varepsilon_\infty (\frac{\omega_{LO}^2}{\omega_{TO}^2} - 1))$ is an oscillator strength and Γ the phonon damping; ω_{LO} , ω_{TO} phonon frequencies are related to the well-known Lyddane-Sachs-Teller (LST) relationship via ω_{LO} $[\equiv \omega_{TO} \left(\frac{\varepsilon_o}{\varepsilon_\infty}\right)^{1/2}]$.

For ternary alloys [e.g., $(AB_{1-x}C_x)$ with A = Te, B = Be, C= Zn], the composition dependent $\tilde{\varepsilon}_x(\omega)$ (cf. Eq. (1)) can be re-written as a superposition of the two AB and AC-like (j = 1, 2) damped harmonic oscillators [19]:

$$\tilde{\varepsilon}_x(\omega) = \varepsilon_{\infty x} \left[1 - \frac{\omega_P^2}{\omega^2 + i\omega\gamma}\right] + \sum_{j=1,2} \frac{S_{jx}\omega_{TOjx}^2}{\omega_{TOjx}^2 - \omega^2 - i\omega\Gamma_{jx}} , \quad (2)$$

where the term $\varepsilon_{\infty x} (\equiv \varepsilon_{\infty 1} + (\varepsilon_{\infty 2} - \varepsilon_{\infty 1}).x)$ represents high frequency dielectric constant taken as a weighted average between the corresponding values of pure BeTe and ZnTe; S_{jx} is x dependent oscillator strength; ω_{TOjx} and Γ_{jx} represent, respectively, the resonance frequency and damping constant of the j^{th} ω_{TO} phonon for different x.

The values of ε_∞, ω_{TO}, Γ, and S (cf. Table 1) for the bulk materials are the fitting parameters (cf. Sec. 3) used in the Drude-Lorentz model (cf. Eq. (1)). The quantities including plasmon (ω_P) frequency in p-BeTe, and its damping constant are carefully evaluated by minimizing the mean-squares deviations using a regression program. Once the $\tilde{\varepsilon}(\omega)$ is accurately constructed for each material, the reflectance coefficient $\tilde{r}$ at near normal incidence can be obtained:

$$\tilde{r} = \frac{1-\sqrt{\tilde{\varepsilon}(\omega)}}{1+\sqrt{\tilde{\varepsilon}(\omega)}}\ , \qquad (3)$$

to model the power reflection $R(\omega) = |\tilde{r}|^2$.

2.2 Reflectivity and transmission spectra in thin epifilms

In the FIR spectroscopy [16], a polar film of thickness *d* is considered thin if $\omega/c >> d$ (or equivalently $\lambda >> d$) with ω being the frequency of incident EM wave and *c* is the speed of light. In such films one can distinguish two uniform normal modes of vibrations: one with atomic motions parallel to the plane of the film (ω_{TO} modes) and the other having atomic motions perpendicular to the plane of the film (ω_{LO} modes).

For simulating the reflectivity of BeTe/GaAs (001), ZnTe/GaAs (001), $Be_xZn_{1-x}Te$/GaAs (001) epifilms with thickness *d*, we have adopted a standard methodology of multilayer optics in the framework of a three phase (ambient/film/substrate) model. The amplitude of reflection coefficient $\tilde{r}_{123}$ or reflectivity $R(\omega) = |\tilde{r}_{123}|^2$ at near normal incidence can be calculated by using [19]:

$$\tilde{r}_{123} = \frac{\tilde{r}_{12}+\tilde{r}_{23}\exp(2i\beta)}{1+\tilde{r}_{12}\tilde{r}_{23}\exp(2i\beta)}\ , \qquad (4)$$

where $\tilde{r}_{12} = \frac{1-\tilde{n}_2}{1+\tilde{n}_2}$; $\tilde{r}_{23} = \frac{\tilde{n}_2-\tilde{n}_3}{\tilde{n}_2+\tilde{n}_3}$ with $\tilde{n}_2 = \sqrt{\tilde{\varepsilon}_2}$ and $\tilde{n}_3 = \sqrt{\tilde{\varepsilon}_3}$ are the Fresnel coefficients. The term $\beta = 2\pi d\frac{\sqrt{\tilde{\varepsilon}_s(\omega)}}{\lambda}$ in Eq. (4) represents the phase multiplier with $\tilde{\varepsilon}_s(\omega)$ being the dielectric constant of the substrate and λ is the wavelength of the incident light. An expression (like Eq. (4)) for the transmission coefficient $\tilde{t}_{123}$ at near normal incidence can be derived [19].

2.2.1 Berreman's effect

The articulation to simulate the reflectivity $R(\omega) = |\tilde{r}_{123}|^2$ (transmission $T(\omega) = |\tilde{t}_{123}|^2$) at oblique incidence angle θ_i [17] is, however, a little more involved. If the EM wave is incident on the film with electric field polarized perpendicular to the plane of incidence [i.e., the s-wave], the radiation only interacts with the ω_{TO} modes regardless of the angle of incidence θ_i. In contrast, both ω_{TO} and ω_{LO} modes are excited by radiation that impinges on the film at an angle θ_i with electric field polarized parallel to the plane of incidence [i.e., the p-wave] i.e., the BE effect. In such a situation, the electric field has a component in the direction of the atomic motions for both the ω_{TO} and ω_{LO} phonons.

This simple and elegant method was first introduced by Berreman [17] by using FIR transmission at oblique incidence on a thin LiF prepared on a collodion film. The BE method has clearly demonstrated its elegance and ease of exercising – the only restriction is that the film must be thinner than the wavelength of EM radiation corresponding to that of the Reststrahlen band. In many epitaxially grown films, MQWs and SLs, this condition can be easily maintained [5-8]. One must note that there exist no FIR measurements at oblique-incidence for the MBE grown undoped binary or doped $Be_xZn_{1-x}Te$/GaAs epifilms and BeTe/ZnTe/GaAs SLs. Here, we have reported the results of our systematic calculations of the reflectivity/transmission spectra by exploiting a three-phase model in the multilayer optics approach [19].

3. Numerical simulations results and discussion

The calculation of $\tilde{\varepsilon}(\omega)$ for different materials is the foundation of relating the optical phonon frequencies to their reflectivity spectrum. By using Eqs. (1-2), we have carried out least square fit to the reflectivity of ZnTe, BeTe, $Be_{0.5}Zn_{0.5}Te$, and GaAs [21-25] by exploiting the CERN library MINUIT program based on Metropolis algorithm to obtain the necessary phonon mode parameters (see: Table 1). For thin epifilms and SLs the reflectance and transmission spectra in the s- and p-polarized configurations are obtained by using the interference matrix approach [19]. The type of formalism that we have adopted here gives the transmission results similar to those obtained by Berreman for a single LiF film [17]. However, our method can be applied to a structure of arbitrary number of layers, one of which could be a substrate. Theoretical details used here to calculate the reflectivity/transmission spectra at oblique-incidence for BeTe, ZnTe and $Be_xZn_{1-x}Te$ epifilms on GaAs substrate are reported elsewhere [20].

3.1 Reflectivity spectra of bulk materials

By exploiting the parameter values from Table 1, the simulated results of FIR reflectance spectra are displayed in Fig. 1 for the bulk materials. Different colored lines are used to discriminate the spectra of ZnTe, $Be_{0.5}Zn_{0.5}Te$, BeTe and GaAs. The vertical arrows of distinctive colors (e.g., sky blue, grey, magenta, and black) are drawn to signify their respective Reststrahlen band regions. The perusal of Fig. 1 clearly reveals that the spectrum of each binary material drops to a minimum value at the plasma edge and exhibits a peak near the ω_{TO} phonon frequency. As expected, the calculated spectra of ternary $Be_{0.5}Zn_{0.5}Te$ alloy (green color line) demonstrated two Reststrahlen peaks one each related to the ZnTe- and BeTe-like phonon regions, respectively.

3.2 BE in thin epilayers and superlattices

Although the Raman spectroscopy is considered as a highly credible method for exploring the optical phonons of polar materials [13], many researchers have relied, however, using the FIR reflectance measurements [14]. In contrast, very few reports exist exploiting the transmission spectroscopy at $\theta_i \neq 0$ [16] as most FIR studies are performed at a near normal incidence (i.e., θ_i = 0). Following the methodology outlined in Sec. 2.2 and using the phonon-mode parameters from Table 1, we have calculated the reflectance and transmission spectra at oblique incidence θ_i ($\equiv 45^o$) for BeTe/GaAs (001) (cf. Sec. 3.2.1), ZnTe/GaAs (001) (cf. Sec. 3.2.2), $Be_{0.5}Zn_{0.5}Te$/GaAs (001) (cf. Sec. 3.2.3) epifilms and BeTe/ZnTe/GaAs (001) SL (cf. Sec. 3.2.4).

3.2.1 BeTe/GaAs (001)

In Fig. 2 a)), we have reported the results of our simulated reflectivity (red and blue color lines: lower panel) and transmission spectra (green and black color lines: upper panel), respectively in the s- and p-polarization for a BeTe/GaAs (001) epifilm of thickness d ($\equiv 0.1$ μm) at an incidence angle θ_i ($\equiv 45^o$). Clearly, the spectral outcomes (see: Fig. 2 a)) can be divided into two parts: (a) the BeTe-like phonon region which falls between the mode frequencies of ~ 460 to ~505 cm^{-1} and, (b) a broad GaAs-like Reststrahlen band of the substrate occurring in the range of ~268 to ~295 cm^{-1}. While the reflectivity spectra of GaAs shown by sky blue color vertical arrows remained nearly unaffected, the transmission and reflectivity of BeTe-bands indicated by magenta color vertical arrows, are, however, seen changing significantly in the s- and p-polarizations. Obviously, our simulations of $R_p(\omega)/(T_p(\omega))$ spectra in the p-polarization of BeTe/GaAs (001) epilayer (see: Fig. 2 a)) have confirmed ω_{TO} mode appearing at ω_{TO}^{BeTe}~ 461 cm^{-1} as a distinct maximum (minimum). In addition, a sharp minimum is seen emerging at a higher frequency indicating the ω_{LO} mode at ω_{LO}^{BeTe}~503 cm^{-1}. In the s-polarization, however, the simulated $R_s(\omega)/(T_s(\omega))$ spectra revealed only the ω_{TO} mode as a maximum (minimum) in excellent agreement with the Raman scattering results [13].

3.2.2 ZnTe/GaAs (001)

In Fig. 2 b)), we have reported our calculated results of reflectivity (red and blue color lines: lower panel) and transmission spectra (green and black color: upper panel), respectively in the s- and p-polarization for a ZnTe/GaAs (001) epifilm of thickness d ($\equiv 0.1$ μm) at an incidence angle

θ_i (≡ 45°). Like BeTe/GaAs (001), the reflectivity spectra in s- and p-polarization of ZnTe/GaAs (001) also exhibited two regions: (a) a broad GaAs-like Reststrahlen band region of the substrate indicated by the sky-blue color vertical arrows occurring in the frequency range of ~268 to ~295 cm^{-1} and, (b) a ZnTe-like phonon region which falls between the mode frequencies of ~ 175 to ~205 cm^{-1}. While the reflectivity spectra of GaAs shown by sky blue color vertical arrows remained nearly unaffected, the transmission and reflectivity spectra of ZnTe-bands indicated by magenta color arrows are, however, perceived changing significantly in the s- and p-polarizations. Obviously, the simulations of $R_p(\omega)/(T_p(\omega))$ spectra in p-polarization for ZnTe/GaAs (001) epilayer (see: Fig. 2 b)) confirmed the ω_{TO} mode appearing at ω_{TO}^{ZnTe}~ 177 cm^{-1} as a distinct maximum (minimum). In addition, a sharp minimum is also seen emerging at a higher frequency indicating the ω_{LO} mode at ω_{LO}^{ZnTe}~207 cm^{-1}. In s-polarization the simulated $R_s(\omega)/(T_s(\omega))$ spectra, however, revealed only the ω_{TO} mode as a maximum (minimum) in excellent agreement with the INS [12] and Raman scattering [13] results.

3.2 .3 $Be_{0.5}Zn_{0.5}Te$/GaAs (001)

Like BeTe/GaAs (001) and ZnTe/GaAs (001) epifilms (cf. Secs. 3.2.1-3.2.2), we have also reported in Fig. 2 c) our simulated results of the reflectivity and transmission spectra in the s- and p-polarization for a $Be_{0.5}Zn_{0.5}Te$/GaAs (001) epilayer of thickness d (≡ 0.2 μm) at an oblique incidence θ_i (≡ 45°). Unlike binary materials (cf. Figs. 2 a) – 2 b)), the calculated results of FIR reflectivity (red and blue color lines: lower panel) and transmission spectra (green and black color lines: upper panel) of $Be_{0.5}Zn_{0.5}Te$ alloy epifilm exhibit three regions: (a) a broad GaAs-like Reststrahlen band region indicated by sky-blue color vertical arrows occurs in the frequency range of ~268 to ~295 cm^{-1}, (b) the ZnTe-like phonon region shown by magenta color vertical arrows falls between the mode frequencies of ~180 to ~205 cm^{-1}, and (c) the BeTe-like phonon region indicated by grey colored vertical arrows appears in the mode frequency range of ~430 to ~465 cm^{-1}. While the reflectivity spectra of GaAs shown by sky blue color vertical arrows remained nearly unaffected, the transmission and reflectivity of ZnTe-bands indicated by magenta color arrows, and BeTe-bands shown be grey color arrows are, however, perceived changing significantly in the s- and p-polarizations. Once again, our results of p-polarized $R_p(\omega)/(T_p(\omega))$ spectra for $Be_{0.5}Zn_{0.5}Te$/ GaAs (001) epilayer (see: Fig. 2 c)) have confirmed ω_{TO} modes emerging as distinct maximum (minimum) at ω_{TO}^{ZnTe}~ 189.8 cm^{-1} and ω_{TO}^{BeTe}~ 437.7 cm^{-1}, respectively. In

addition, the sharp minima appear at higher frequencies indicating the ω_{LO} modes of ω_{LO}^{ZnTe}~204.2 cm^{-1} and ω_{LO}^{BeTe}~463.1 cm^{-1}, respectively. In s-polarization, however, the calculated $R_s(\omega)/(T_s(\omega))$ spectra revealed only the ω_{TO}^{ZnTe}, ω_{TO}^{BeTe}modes as a maximum (minimum) in excellent agreement with the INS [12] and Raman scattering [13] data.

3.2.4 BeTe/ZnTe/GaAs (001) superlattice

The multilayer optics for calculating the reflectivity and transmission spectra of thin films at oblique incidence has been extended to SLs [19]. In the long wavelength limit, the dielectric function $\tilde{\varepsilon}_{SL}$ of the SL is a diagonal tensor whose components can be written as a weighted average of the dielectric functions $\tilde{\varepsilon}_{AB}$ and $\tilde{\varepsilon}_{AC}$ of the constituent materials *AB* and *AC* having thicknesses d_{AB}, d_{AC} {19]:

$$\tilde{\varepsilon}_{SL}(\omega) = \left[\frac{\tilde{\varepsilon}_{AB}(\omega)\,\delta+\tilde{\varepsilon}_{AC}(\omega)}{\delta+1}\right], \qquad (5)$$

where $\delta = \frac{d_{AB}}{d_{AC}}$.

In Fig. 2 d) the results of reflectance and transmission spectra are reported for the BeTe/ZnTe /GaAs (001) in s- and p-polarization at θ_i (= 45°) of SL period d (≡ $d_{AB} + d_{AC}$) having d_{AB} (≡ 50 Å); d_{AC} (≡ 100 Å) with a stacking period of 25. Like ternary alloy $Be_{0.5}Zn_{0.5}Te$ (cf. Fig. 2 c)), the reflectivity (red and blue color lines: lower panel) and transmission spectra (green and black color lines: upper panel) of the SL (see: Fig. 2 d) can be divided into three regions: (a) a broad GaAs-like Reststrahlen band region indicated by sky-blue color vertical arrows occurs in the frequency range of ~268 to ~295 cm^{-1}, (b) a ZnTe-like phonon frequency region shown by magenta color vertical arrows falls between ~175 to ~205 cm^{-1}, and (c) a BeTe-like phonon band shown by grey color vertical arrows appears in the frequency region of ~430 to ~465 cm^{-1}.

Since the optical mode frequencies of bulk materials BeTe (ω_{LO1}, ω_{TO1}) and ZnTe (ω_{LO2}, ω_{TO2}) are well separated, these phonons in BeTe/ZnTe SLs are expected to be confined in their respective layers. The calculations of $R_p(\omega)/(T_p(\omega))$ spectra (cf. Fig. 2 d)) in the p-polarization have confirmed BeTe-like (ω_{LO1} (~503 cm^{-1}), ω_{TO1} (~461 cm^{-1})) and ZnTe-like (ω_{LO2} (~205 cm^{-1}), ω_{TO2} (~179 cm^{-1})) modes. The simulations of $R_s(\omega)/(T_s(\omega))$ spectra in the s-polarization have identified, however, only the ω_{TO1} and ω_{TO2} modes. Our recent study of layer-dependent Raman intensity profiles in $(BeTe)_m/(ZnTe)_n$ SLs [49] have substantiated the observation of confined

optical modes with a slight upward shift of ZnTe-like phonon as noticed in the reflectivity/ transmission study.

3.3 BE in doped materials

In N-doped BeTe epifilm, one would expect ω_{LO}^{BeTe} phonon to strongly couple [50-55] with the collective oscillations of free-carriers (plasmons). This coupling of longitudinal optical phonon plasmon (LOPL) depends on η - it is maximum when the two [i.e., ω_{LO}^{BeTe} and $\omega_{\pm}^{*}$] modes have comparable frequencies. In the long wavelength limit, the LOPL mode frequencies in p-BeTe can be obtained from the zeros of dielectric response function $\tilde{\varepsilon}(\omega)$ (Eq. 1). The terms ω_{+}^{*} and ω_{-}^{*} are complex and their real parts (i.e., $\omega_{LOPL}^{+} \equiv \text{Re}\ \omega_{+}^{*}$ and $\omega_{LOPL}^{-} \equiv \text{Re}\ \omega_{-}^{*}$) provide the two branches (see: Fig. (3 a)): an upper ω_{LOPL}^{+} and lower ω_{LOPL}^{-} branch for a given η (or plasma frequency ω_p). In doped semiconductors, the $\omega_{LOPL}^{\pm}$ modes are usually detected by Raman scattering spectroscopy, the optical exposure of such modes by infrared reflectivity at oblique incidence (cf. Sec. 3.3.1) is also possible [56-59].

3.3.1 p-BeTe/GaAs (001)

As stated before, in p-BeTe we expect strong coupling between ω_{LO}^{BeTe} phonons and plasmons. In Fig. 3 a) we have reported the calculated ω_P and coupled $\omega_{LOPL}^{\pm}$ mode frequencies as a function of η. At different doping levels η, the simulated results of transmission $[T_s(\omega)/T_p(\omega)]$ and reflectance $[R_s(\omega)/R_p(\omega)]$ spectra are displayed in Figs. 3 b) and 3c), respectively for a 0.5 μm thick p-type BeTe/GaAs (001) at oblique incident angle ($\theta_i = 45^o$). From Fig. 3b) (Fig. 3 c)), we noticed that the minima (maxima) in $T_s(\omega)$ ($R_s(\omega)$ linked to ω_{TO}^{BeTe} modes are asymmetrically broadened – possibly by the increase of free-carrier concentration. The other features perceived in $T_p(\omega)/R_p(\omega)$ spectra are the dips (indicated by grey color vertical arrows) at higher frequencies which shift towards higher frequency with the increase of η. One must note that the transmission (reflection) minima near ~524.4 cm^{-1}, ~528.3 cm^{-1}, and ~532.7 cm^{-1} in Figs. 3 b) and 3 c) are not perceived in the s-polarization $[T_s(\omega)/ R_s(\omega)]$ and we assign these structures as ω_{LOPL}^{+} modes based on their dependence on carrier concentration η, and appearance only in the p-polarization spectra. This assignment is further supported by the calculations carried out for ω_{LOPL}^{+} mode frequencies derived from the zeros of the real part of $\tilde{\varepsilon}(\omega)$ (Eq. 1) with $\gamma = 0$, $\Gamma = 0$. Again, we are

unable to identify the features related to ω_{LOPL}^{-} modes. This result is not surprising as ω_{LOPL}^{-} mode being plasmon-like at lower η has a relatively large damping constant [56-59] and weaker strength while at higher η it is expected to merge with a stronger and broader ω_{TO}^{BeTe}phonon minimum. On the other hand, with larger plasmon contribution at higher η, the ω_{LOPL}^{+} mode in p-BeTe though broad is distinctly noticeable (cf. Figs. 3b-3c).

3.4 BE and MREI model in $Be_{1-x}Zn_xTe$

To corroborate the observed two-phonon-mode behavior in $Be_{1-x}Zn_xTe$ alloys, it is required to have accurate x-dependent ω_{TO} and ω_{LO} phonons. From the existing Raman scattering results of $Be_{1-x}Zn_xTe$ [13] one may note that the BeTe-like phonons decrease with an increase of Zn composition, x. On the other hand, the ZnTe-like ω_{LO}-ω_{TO} phonons demonstrate a different behavior as a function of x. Since ω_{LO} modes are not observed in the FIR reflectivity at near normal incidence their frequencies are usually obtained from the maxima of energy-loss function –Im($1/\tilde{\varepsilon}$) [i. e., $\omega_{LO}^2 = {S\omega_{TO}^2}/{\varepsilon_\infty} + \omega_{TO}^2$]. In ternary $Be_{1-x}Zn_xTe$ alloys, as x is increased, the ω_{LO}-ω_{TO} splitting of BeTe- modes and their oscillator strength S decreases methodically. One may also note similar behavior of the mode splitting ω_{LO}-ω_{TO} and S by decreasing x for ZnTe-like phonons. At the limiting values of $x \rightarrow 0$ (or $x \rightarrow 1$) the ω_{LO}-ω_{TO} splitting of ZnTe-like (BeTe-like) modes reduces to zero. Consequently, one would expect (see Table 2 and Fig. 4) observing a gap mode of Zn in *Be*Te (or a localized vibrational mode (LVM) of Be in *Zn*Te). By using BE, we have demonstrated (cf. Secs.3.2.1-3.2.3) that it is possible to achieve accurate values of ω_{LO}, ω_{TO} phonons for both binary and ternary alloys. In $Be_{1-x}Zn_xTe$ alloys, we strongly feel that BE can be used to confirm the two-phonon mode behavior (cf. Sec. 3.4.1).

3.4.1 MREI model

Earlier, the MREI model has been applied successfully to verify the observed two-phonon mode behavior in many semiconducting ternary alloys including CdS_xSe_{1-x} [60], $Zn_xCd_{1-x}Te$ [61], and $CuCl_{1-x}Br_x$ [62], etc. By using the parameter values of Table 2, we have displayed in Fig. 4 our calculated MREI results of composition dependent long wavelength optical phonon frequencies of $Be_{1-x}Zn_xTe$ for $0 \leq x \leq 1$. The agreement with the existing Raman scattering results [13] for the Zn-rich region as well as the optical modes (ω_{LO2}, ω_{TO2}) and (ω_{LO1}, ω_{TO1}) derived by using BE for the $Be_{0.5}Zn_{0.5}Te$ is quite satisfactory.

4. Conclusions

In summary, we have reported the results of comprehensive simulations for the FIR reflectivity /transmission spectra at near normal ($\theta_i = 0$), and oblique incidence ($\theta_i \neq 0$) (i.e., BE configuration) to assess the optical phonons in undoped/doped epilayers of binary BeTe (ZnTe)/GaAs (001), ternary $Be_{0.5}Zn_{0.5}Te$ /GaAs (001) alloys and BeTe/ZnTe/GaAs (001) SLs. The study has provided accurate values of ω_{TO} and ω_{LO} phonons comparable to the complementary Raman scattering spectroscopy data [13]. In the absence of experimental results of vibrational mode characteristics in ternary alloys, the BE and Greens function methodologies [45] can be valuable for assessing the x-dependent optical phonons and LVMs/gap modes at $x \rightarrow 1/x \rightarrow 0$, respectively for predicting their phonon mode behaviors. In p-doped BeTe/GaAs epilayers, the calculated $T_p(\omega)$/ $R_p(\omega)$ spectra have not only validated the LO-plasmon coupled ω^{+}_{LOPL} modes exhibiting longitudinal character but also demonstrated their appropriate shift towards higher frequency by increasing the charge carrier concentration η. Infrared reflectance measurements have been used earlier in doped polar materials to assess the electron charge density [56-59]. We strongly believe that a careful assessment of ω^{+}_{LOPL} modes by polarization dependent FIR spectroscopy is an alternative, elegant and quite effective method, complementary to the Raman scattering spectroscopy for estimating the free-carrier density η in doped polar semiconductor epilayers.

Acknowledgements

The author (DNT) wishes to thank Dr. Deanne Snavely, Dean College of Natural Science and Mathematics at Indiana University of Pennsylvania (IUP) for the travel support and the Innovation Grant that he received from the School of Graduate Studies making this research possible.

Declarations

Conflict of interest

The authors have no competing interests to declare that are relevant to the content of this article.

Availability of data

Data is available from the corresponding author with a reasonable request

References

1. II-VI Semiconductor materials and their applications, Edited by Maria C. Tamargo (Taylor Francis, 2002); O. Maksimov, S.P. Guo, M. Munoz and M.C. Tamargo, Optical properties of BeCdSe/ZnCdMgSe strained quantum well structures, J. Appl. Phys. **90**, 5135 (2001); O. Maksimov and M.C. Tamargo, Direct-to-indirect band gap crossover for the $Be_xZn_{1-x}Te$ alloy, Appl. Phys. Lett. **79**, 782 (2001); S.P. Guo, Y. Luo, W. Lin, O. Maksimov, M.C. Tamargo, I. Kuskovsky, C. Tian, G.F. Neumark, High crystalline quality ZnBeSe grown by molecular beam epitaxy with Be–Zn co-irradiation, Journal of Crystal Growth **208**, 205-210 (2000).

2. O. Maksimov, Beryllium chalcogenide alloys for visible light emitting and laser diodes, Rev. Adv. Mater. Sci. **9**, 178 (2005).

3. J. S. de Almeida and R. Ahuja, Tuning the structural, electronic, and optical properties of $Be_xZn_{1-x}Te$ alloys Appl. Phys. Lett. **89**, 061913 (2006).

4. A. Waag, F. Fischer, H.J. Lugauer, T. Litz, J. Laubender, U. Lunz, U. Zhender, W. Ossau, T. Gerhardt, M. Moller, and G. Landwehr, Molecular-beam epitaxy of beryllium-chalcogenide-based thin films and quantum-well structures, J. Appl. Phys. **80**, 792(1996).; A. Waag, F. Fischer, K. Schüll, T. Baron, H.-J. Lugauer, Th. Litz, U. Zehnder, W. Ossau, T. Gerhard, M. Keim, G. Reuscher, and G. Landwehr, Laser diodes based on beryllium-chalcogenides, Appl. Phys. Lett. **70**, 280 (1997).; V. Wagner, J. Geurts, T. Gerhard, T. Litz, H.-J. Lugauer, F. Fischer, A. Waag, G. Landwehr, T Walter, D. Gerthsen, Determination of BeTe phonon dispersion by Raman spectroscopy on BeTe/ZnSe-superlattices, Applied Surface Science **123/124**, 580-584 (1998).; T. Walter, A. Rosenauer, R. Wittmann, D. Gerthsen, F. Fischer, T. Gerhard, A. Waag, G. Landwehr, P. Schunk, and T. Schimmel. Structural properties of BeTe/ZnSe superlattices, Phys. Rev. **B 59**, 8114 (1999).; V. Wagner, S. Gundel, J. Geurts, T. Gerhard, T. Litz, H.-J. Lugauer, F. Fischer, A. Waag, G. Landwehr, R. Kruse, C. Becker, U. Kiister, Optical and acoustical phonon properties of BeTe, Journal of Crystal Growth **184/185**, 1067-1071 (1998).; V. Wagner and J. Geurts Raman and Modulation Spectroscopy at II–VI Semiconductor Interfaces, phys. stat. sol. (a) **184**, 29–39 (2001).

5. S. B. Che, I. Nomura, A. Kikuchi, and K. Kishino, Yellow-green ZnCdSe/BeZnTe II-VI laser diodes grown on InP substrates, Appl. Phys. Lett. **81**, 972 (2002).; S. B. Che, I. Nomura, W. Shinozaki, A. Kikuchi, K. Shimomura, K. Kishino, Wide bandgap over 3 eV and high p-doping BeZnTe grown on InP substrates by molecular beam epitaxy, J. Cryst. Growth, **214**, 321 (2000).

6. W. C. Tsai, C. L. Cheng, T. T. Chen, and Y. F. Chen, Investigation of degradation in beryllium chalcogenide II-VI semiconductors, Appl. Phys. Lett. **89**, 121918 (2006); https://doi.org/10.1063/1.2355460

7. S.V. Ivanov, S.V. Sorokin and I.V. Sedova, Molecular Beam Epitaxy. Ch. 27 Elsevier (2013) http://dx.doi.org/10.1016/B978-0-12-387839-7.00027-0

8. M. Anni, Polymer II-VI Nanocrystals blends: Basic Physics and Device Applications to Lasers and LEDs, Nanomaterials, **9**, 1036 (2019).

9. I. Nomura, Y. Sawafuji, and K. Kishino, Photopumped Lasing Characteristics in Green-to-Yellow Range for BeZnSeTe II–VI Compound Quaternary Double Heterostructures Grown on InP Substrates, Jpn. J. Appl. Phys. **50**, 031201 (2011).; I. Nomura, K. Kishino, T. Ebisawa, Shun Kushida, Jun Uota, K. Tasai, H. Nakamura, T. Asatsuma, and H. Nakajima, (IEEE 21st International Semiconductor Laser Conference, 14-18 Sept. 2008 Sorrento. Italy); **DOI:** 10.1109/ISLC.2008.4636070.

10. Y. Zhang**,** G. Deng, Y. Yu, Y. Wang, D. Zhao, Z. Shi, B. Zhang, and X. Li, Demonstration of N-polar III-nitride tunnel junction LED, ACS Photonics**, 7,** 1723 (2020).

11. H. S. Wasisto, J. D. Prades, J. Gulink, and A. Waag, Beyond solid-state lighting: Miniaturization, hybrid integration, and applications of GaN nano- and micro-LEDs Appl. Phys. Rev. **6**, 041315 (2019).

12. N. Vagelatos, D. Wehe and J.S. King, Phonon dispersion and phonon densities of states for ZnS and ZnTe, J. Chem. Phys. **60**, 3613 (1974).

13. O. Pagès, M. Ajjoun, D. Bormann, C. Chauvet, E. Tournié, and J. P. Faurie, Vibrational evidence for a percolative behavior in $Zn_{1-x}Be_xSe$, Phys. Rev. **B 65**, 035213 (2001).; ibid Percolation behavior in the Raman spectra of ZnBeTe alloy, Appl. Phys. Lett. **80**, 3081 (2002); ibid Long-wave phonons in ZnSe-BeSe mixed crystals: Raman scattering and percolation model, Phys. Rev. **B 70**, 155319 (2004).; O. Pagès, T. Tite, D. Bormann, O. Maksimov, and M.C. Tamargo, Percolation behavior in the Raman spectra of ZnBeTe alloy, Appl. Phys. Lett. **80**, 3081 (2002).

14. E. Oh and A.K. Ramdas, Multi-Mode behavior of optical phonons in II-VI ternary and quaternary alloys. J. Electr. Material **23**, 307–312 (1994). https://doi.org/10.1007/BF02670640

15. N. Mandal, F. C. Peiris, O. Maksimov and M. C.Tamargo, Far-infrared dielectric functions and phonon spectra of $Be_xZn_{1-x}Te$ alloys determined by spectroscopic ellipsometry, Sol. Stat, Comm. **149**, 1698 (2009).

16. M. D. Sciacca, A. J. Mayur, E. Oh, A. K. Ramdas, S. Rodriguez, J. K. Furdyna, M. R. Melloch, C. P. Beetz and W. S. Yoo, Infrared observation of transverse and longitudinal polar optical modes of semiconductor films: Normal and oblique incidence, Phys. Rev. **B 51**, 7744 (1995).

17. D. W. Berreman, Infrared Absorption at Longitudinal Optical Frequency in Cubic Crystal Films, Phys. Rev. **130**, 2193 (1963).

18. M. Kurka, M. Rygała, G. Sęk , P. Gutowski, K. Pierscinski, and M. Motyka, Contactless Measurements of Carrier Concentrations in InGaAs Layers for Utilizing in InP-Based Quantum Cascade Lasers by Employing Optical Spectroscopy, Materials **13**, 3109 (2020); doi:10.3390/ma13143109.

19. O. E. Piro, Optical properties, reflectance, and transmittance of anisotropic absorbing crystal plates, Phys. Rev. **B 36**, 3427 (1987).

20. D. N. Talwar, H. H. Lin and Z. C. Feng, Polarization dependent infrared reflectivity studies of Si-doped MOCVD grown GaN/Sapphire epilayers, Mat. Chem. Phys. **252**, 123279 (2020).

21. V. Wagnera, S. Gundel, J. Geurt, T. Gerhard, Th. Litz, H.-J. Lugauer, F. Fischer, A. Waag, G. Landwehr, R. Kruse, Ch. Becker, U. Kiister, Optical and acoustical phonon properties of BeTe, Journal of Crystal Growth **184/185**, 1067-1071 (1998).

22. W. Sen, S. W. Zhong, O. Hirishi and G. Q. Xin, Study of far-infrared reflection and Raman scattering in reactive ion etched ZnTe, Chin. Phys. **12**, 1026 (2003).

23. D. N. Talwar, T. R. Yang Z. C. Feng, and P. Becla, Infrared reflectance and transmission spectra in II-VI alloys and superlattices**,** Phys. Rev. **B 84**, 174203 (2011).

24. S. Perkowitz, L. S. Kim, Z. C. Feng, and P. Becla, Optical phonons in $Cd_{1-x}Zn_xTe$, Phys. Rev. **B 42**, 1455 (1990).

25. A. A. Wronkowska, H. Arwin, F. Firszt, S. Legowski, A. Wronkowski and L. Skowronski, Optical spectra of $Zn_{1-x}Be_xT$emixed crystals determined by IR-VIS-UV ellipsometry, Thin Solid Films. **519**, 2795 (2011).

26. P. Giannozzi, S. de Gironocoli, P. Pavone and S. Raroni, Abinitio calculation of phonon dispersions in semiconductors, Phys. Rev. **B 43**, 7231 (1991).

27. S.Q. Wang and H.Q. Ye, First-principles study on elastic properties and phase stability of III–V compounds, Phys. Stat. Sol. **(b) 240,** 45 (2003).

28. Gökhan Gökoglu, Theoretical investigation of zincblende AlSb and GaSb compounds J. Alloys Comp. **478,** 653–656 (2009).

29. L. Zhang, J. T-Thienprasert, M.-H. Du, D. J. Singh, and S. Limpijumnong, Comment on Spectroscopic Signatures of Novel Oxygen-Defect Complexes in Stoichiometrically Controlled CdSe, Phys. Rev. Lett. 102, 209601 (2009); J. T. Thienprasert, S. Limpijumnong, A. Janotti, C. G. Van de Waal, L. Zhang, M.-H. Du, and D. J. Singh, Vibrational signatures of O_{Te} and O_{Te} –V_{Cd} in CdTe: A first-principles study, Comp. Mat. Sci. **49**, S245 (2010).

30. E. A. Vinogradov, B. N. Marvin, N. N. Novikova, V. A. Yukavlev and D. M. Popova, Lattice dynamics of $ZnSe_xS_{1-x}$ semiconductor crystals, Laser Physics, **19**, 162 (2009).

31. T. R. Paudel and W. R. L. Lambrecht, Computational study of phonon modes in short-period AlN/GaN superlattices, Phys. Rev. **B 80**, 104202 (2009). DOI:10.1103/PhysRevB.80.104202 and references cited there.

32. V. Davydov, E. M. Roginskii, Y. Kitaev, A. Smirnov, I. Eliseyev, E. Zavarin, W. Lundin, D. Nechaev, V. Jmerik, M. Smirnov, M. Pristovsek and T. Shubina, The Effect of Interface Diffusion on Raman Spectra of Wurtzite Short-Period GaN/AlN Superlattices, Nanomaterials **11**, 2396 (2021). https:// doi.org/10.3390/nano11092396 and references cited there.

33. Y. Bouhadda, A. Bentabet, N. E. Fenineche,and Y. Boudouma, The *Ab initio* calculation of the dynamical and the thermodynamic properties of the zinc blende GaX (X=N, P, As and Sb) Inter. J. Comp. Mater. Sci. and Eng. **1**, 1250026 (2012).

34. Y. Shen, Y. Yu, X. Kong, J. Deng, X. Tian and Y. Liang, Structural, lattice dynamics and thermodynamic properties of $GaAs_{1-x}P_x$ from first-principles calculations, J. Alloy Comp. **817**, 152733 (2020).

35. S. N. Khatami and Z. Aksamija, Lattice Thermal Conductivity of the Binary and Ternary Group-IV Alloys Si-Sn, Ge-Sn, and Si-Ge-Sn, Phys. Rev. Appl. **6**, 014015 (2016).

36. S. H. Nasrollahi and D. D. Vvedensky, Local normal modes and lattice dynamics, J. App. Phys. **124**, 045102 (2018).

37. T. K. Gajaria, S, D. Dabhi and P. K. Jha, *ab initio* Energetics and Thermoelectric Profiles of Gallium Pnictide Polytypes, Sci. Rep. **9**, 5884 (2019).

38. Y. Mao, X.X. Liang, G.J. Zhao and T.L. Song, The structural and optical properties of ternary mixed crystals $In_xGa_{1-x}As$ with zinc-blende structure by first-principles calculations, Physica B Cond. Matter **509**, 87-95 (2019).

39. K. Kunc, Dynamique de réseau de composés A^NB^{8-N} présentant la structure de la blende, Ann. Phys. (Paris) **8**, 319 (1973-74).

40. P. B. Klein and R. K. Chang, Comparison of second-order Raman scattering measurements with a phonon density-of-states calculation in GaSb, Phys. Rev. **B 14**, 2498 (1976).

41. P. Plumelle and M. Vandevyver, Lattice dynamics of ZnTe and CdTe, Phys. Stat, Sol. **73**, 271 (1976).

42. M. Vandevyver and P. Plumelle, Local force variations due to substitution impurities in nine compounds with the zinc-blende structure, Phys. Rev. **B 17**, 675 (1978).

43. Y. S. Raptis, E. Anastassakis and G. Kanellis, Second-order Raman scattering in AlSb Phys. Rev. **B 46**, 15801 (1992).

44. D. N. Talwar, M. Vandevyver, K. Kunc, and M. Zigone, Lattice dynamics of zinc chalcogenides under compression: Phonon dispersion, mode Grüneisen, and thermal expansion, Phys. Rev. **B 24**, 741 (1981).

45. M. Vandevyver and D. N. Talwar, Green's-function theory of impurity vibrations due to defect complexes in elemental and compound semiconductors, Phys. Rev. **B 21**, 3405 (1980).

46. D. N. Talwar, M. Vandevyver and M. Zigone, Impurity induced Raman scattering spectra in zincblende-type crystals: application to mixed indium pnictides, J. Phys. **C 13**, 3775 (1980).

47. D. N. Talwar and M. Vandevyver, Vibrational structure of copper and zinc complexes in GaAs: A theoretical analysis, Phys. Rev. **B 25**, 6317 (1982).

48. D. N. Talwar, Symmetry adapted impurity modes in as grown n-type GaP:X and GaSb:X (X = S, Se and Te), Comp. Mat. Sci. **204**, 111174 (2022).

49. D. N. Talwar, S. Semone and P. Becla, Comparative study of interfacial strain dependent phonon localization in the beryllium-zinc chalcogenide superlattices, Mat. Chem Phys. **277**, 125523 (2022).

50. A. Mooradian and G. B. Wright, Observation of the Interaction of Plasmons with Longitudinal Optical Phonons in GaAs**,** Phys. Rev. Lett. **16**, 999 (1966).

51. J. Ibánez, Enver Tarhan, A. K. Ramdas, S. Hernández, R. Cuscó, L. Artús, M. R. Melloch and M. Hopkinson, Direct observation of LO phonon-plasmon coupled modes in the infrared transmission spectra of *n*-GaAs and n−$In_xGa_{1-x}As$ epilayers, Phys. Rev. **B 69**, 075314 (2004).

52. C. K. N. Patel and R. E. Slusher, Light Scattering by Plasmons and Landau Levels of Electron Gas in InAs**,** Phys. Rev. **167**, 413 (1968).

53. S. Buchner and E. Burstein, Raman Scattering by Wave-Vector—Dependent LO-Phonon—Plasmon Modes in n-InAs, Phys. Rev. Lett. **33**, 908-911 (1974).

54. Y. B. Li, I. T. Ferguson, R. A. Stradling and R. Zallen, Raman scattering by plasmon-phonon modes in highly doped n-InAs grown by molecular beam epitaxy, Semicond. Sci. Technol. 7, 1149-1154 (1992).

55. Aaron Gregg Lind, Ph. D Thesis, University of Florida (2015); A. G. Lind,T. P. Martin, Jr., V. C. Sorg, E. L. Kennon, V. Q. Truong, H. L. Aldridge, C. Hatem, M. O. Thompson, and K. S. Jones, Activation of Si implants into InAs characterized by Raman scattering, J. Appl. Phys. 119, 095705 (2016).

56. K. H. Eckstein, F. Hirsch, R. Martel, and T. Hertel, Infrared Study of Charge Carrier Confinement in Doped (6,5) Carbon Nanotubes, The Journal of Physical Chemistry **C 125**, 5700-5707 (**2021**) DOI: 10.1021/acs.jpcc.1c00123

57. M. Lewin, C. Baeumer, F. Gunkel, A. Schwedt, F. Gaussmann, J. Wueppen, P. Meuffels, B. Jungbluth, J. Mayer, R. Dittmann, R. Waser, and T. Taubner, Nanospectroscopy of Infrared Phonon Resonance Enables Local Quantification of Electronic Properties in Doped SrTiO3 Ceramics, Adv. Funct. Mater. 28, 1802834 (2018).

58. J. Chochol, K. Postava, M. Cada, M. Vanwolleghem, M. Micica, L. Halagacka, J. F. Lampin and J. Pištora, Plasmonic behavior of III-V semiconductors in far-infrared and terahertz range, Journal of the European Optical Society-Rapid Publications (2017) 13:13 DOI 10.1186/s41476-017-0044-x

59. E. Calandrini, M. Ortolani, A. Nucara, G. Scappucci, W. M. Klesse, M. Y. Simmons, L. D. Gaspare, M. de Seta, D. Sabbagh, G. Capellini, M. Virgilio and L. Baldassarre, Determination of the free carrier concentration in atomic-layer doped germanium thin films by infrared spectroscopy, J. Opt. **16**, 094010 (2014).

60. M. Gorska and W. Nazarewicz, Application of the Random-Element Isodisplacement Model to Long-Wavelength Optical Phonons in $CdSe_xTe_{1-x}$ Mixed Crystals, Phys. Status Solidi **B 65**, 193 (1974).

61. H. Harada and S. Narita, Lattice Vibration Spectra of $Zn_xCd_{1-x}Te$ Alloys J. Phys. Soc. Jpn. **30**, 1628 (1971).

62. D. N. Talwar and B. K. Ghosh, Phonon mode behavior in mixed cuprous halides Ind. J. Pure AppI. Phys. **10**, 733 (1980).

Table 1. Physical properties of ZnTe, BeTe, $Be_{0.5}Zn_{0.5}Te$ and GaAs used in the construction of dielectric functions (see text) for simulating the FIR reflectivity/transmission spectra at oblique incidence.

Parameters	ZnTe	BeTe	$Be_{0.5}Zn_{0.5}Te$	GaAs
$\omega_{TO}\ (cm^{-1})$	176.9	461.0	438, 190	268.7
$\omega_{LO}\ (cm^{-1})$	206.7	502.0	463, 204	292.1
$\Gamma\ (cm^{-1})$	2.2	3.1	2.0, 2.4	2.4
S	2.66	1.3	0.84, 1.09	1.95
ε_∞	7.28 [a)]	6.9 [a)]	7.14	10.9 [b)]
ε_o	9.94	8.2	9.09	12.85

[a)] Ref. [13] [b)] Ref. [16]

Table 2. Values of the parameters used in the MREI model for fitting [a)] the concentration dependence of the optical modes of $Be_{1-x}Zn_xTe$ (see Fig. 4). The experimental data is taken from Pages et al.[b)] Values of longitudinal-optical ($\omega_{LO(\Gamma)}$) and transverse-optical ($\omega_{TO(\Gamma)}$) mode splitting obtained by using Berreman's effect at x = 0.5 (see text). Local vibrational (*Zn*Te:Be) and gap modes (*Be*Te:Zn) are estimated from the Green's function theory [c)] (unpublished) are carefully incorporated in the MREI model [62] to validate the two-phonon mode behavior of ternary alloys (see text).

MREI model parameters [a)] of $TeBe_{1-x}Zn_x$ with Te = A, Be = B, and Zn = C

AB ε_∞ = 6.9
AB $\omega_{LO(\Gamma)}$ = 503 cm^{-1}
AB $\omega_{TO(\Gamma)}$ = 461 cm^{-1}
ω_{gap} = 195 cm^{-1}
Z_{AB}= 0.48
$f_0^{AB} = 0.121E + 06$ dyn/cm
AC ε_∞ = 7.28
AC $\omega_{LO(\Gamma)}$ = 205 cm^{-1}
AC $\omega_{TO(\Gamma)}$ = 177 cm^{-1}
ω_{loc} = 411 cm^{-1}
Z_{AC}= 0.66
$f_0^{AC} = 0.143E + 06$ dyn/cm
θ = 0.28
$f_0^{BC} = 0.042E + 05$ dyn/cm

[a)] Our [b)] Ref. [13] [c)] Ref. [45]

Figure Captions

Fig. 1 Calculated reflectivity spectra of bulk ZnTe (blue color), GaAs (brown color), BeTe (red color) and $Be_{0.5}Zn_{0.5}Te$ (green color) materials. Vertical sky blue, black, magenta and grey color vertical arrows represent the reststrahlen band region for ZnTe. GaAs, BeTe and $Be_{0.5}Zn_{0.5}Te$ materials, respectively (see text).

Fig. 2 Simulated polarization dependent transmission (upper panel) and reflectivity (lower panel) spectra of: (*a*) 0.1 μm BeTe/GaAs epifilm, where the sky blue color vertical arrows represent the Reststrahlen region of GaAs (substrate) while magenta color vertical arrows signify the ω_{TO}^{BeTe} and ω_{LO}^{BeTe}phonons, (*b*) 0.1 μm ZnTe/GaAs epifilm, where the sky blue color vertical arrows represent the Reststrahlen region of GaAs (substrate) while magenta color vertical arrows denote the ω_{TO}^{ZnTe} and ω_{LO}^{ZnTe}phonons, (*c*) 0.2 μm $Be_{0.5}Zn_{0.5}Te$/GaAs epifilm, where the sky blue color vertical arrows represent the Reststrahlen region of GaAs (substrate), magenta color vertical arrows denote the ω_{TO}^{ZnTe}-like and $\omega_{LO}^{ZnTe}-$ like and grey color vertical arrows represent ω_{TO}^{BeTe}-like and $\omega_{LO}^{BeTe}-$ like phonons, and (*d*) $(BeTe)_m/(ZnTe)_n$/GaAs superlattice (see text) where the sky blue color vertical arrows represent the Reststrahlen region of GaAs (substrate), magenta color vertical arrows denote the ω_{TO}^{ZnTe}-like and $\omega_{LO}^{ZnTe}-$ like and grey color vertical arrows represent ω_{TO}^{BeTe}-like and $\omega_{LO}^{BeTe}-$ like phonons (see text).

Fig. 3 (*a*) Simulated carrier concentration dependence of LO- plasmon coupled ($\omega_{LOPL}^{\pm}$) modes in p-BeTe. (*b*) Polarization dependent transmission spectra of 0. 5 μm thick p-BeTe/GaAs epifilms. The first minima shown by vertical grey color arrow in the s-polarization represents ω_{TO}^{BeTe} mode while in the p-polarization besides perceiving first minima representing ω_{TO}^{BeTe} mode the second dip represents ω_{LOPL}^{+}mode which shifts to higher frequency with the increase of η, and (*c*) the polarization dependent reflectance spectra of 0. 5 μm thick p-BeTe/GaAs epifilms where the first maxima shown by vertical grey color arrow in the s-polarization represents ω_{TO}^{BeTe} mode while in the p-polarization besides perceiving the first maxima representing ω_{TO}^{BeTe} mode the second dip represents ω_{LOPL}^{+}mode which shifts to higher frequency with the increase of η (see text).

Fig. 4 Comparison of the MREI model [62] calculations of the two-phonon-mode behavior for $Be_{1-x}Zn_xTe$ with experimental data [13] using parameter values from Table 2. The BE represents (ω_{LO} - ω_{TO}) mode splitting by using Berreman's effect (see: text).

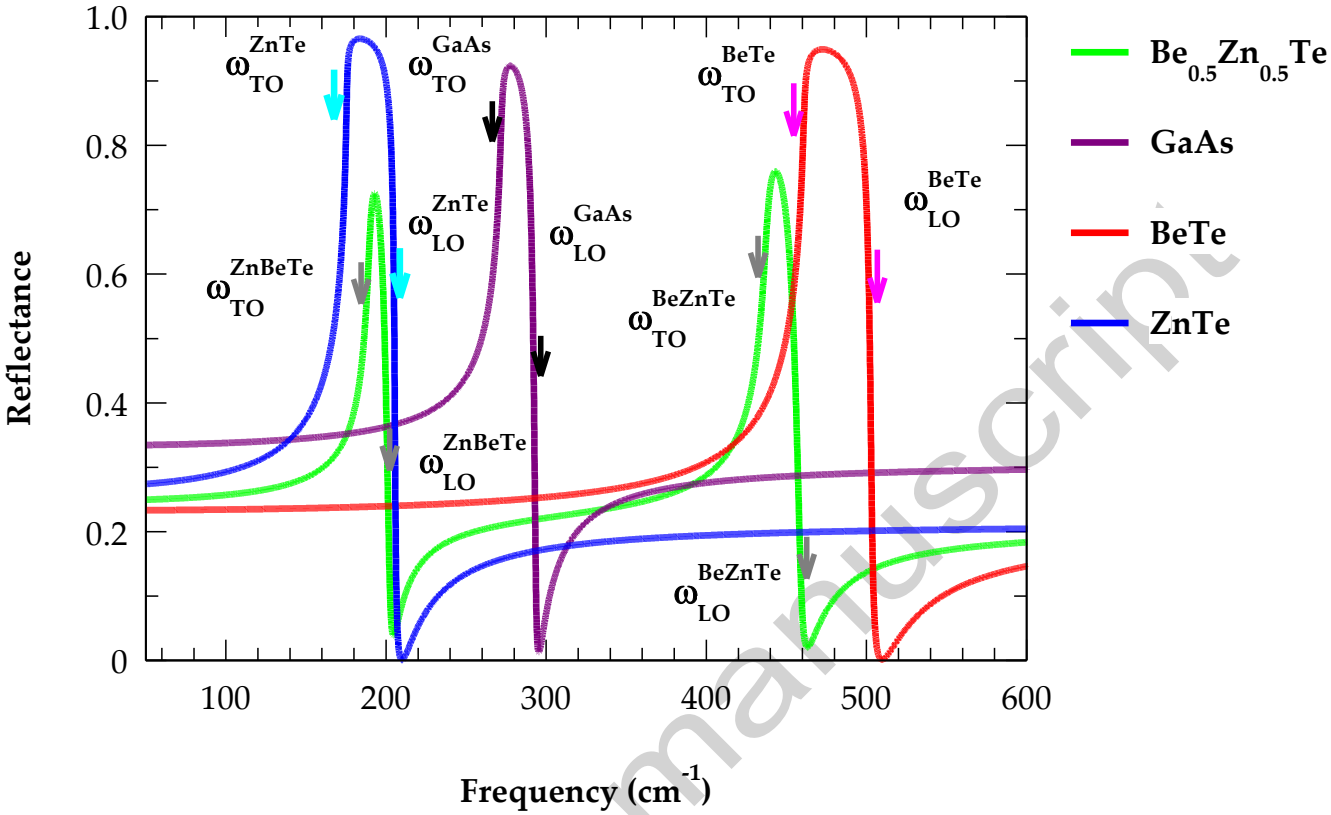

Fig. 1

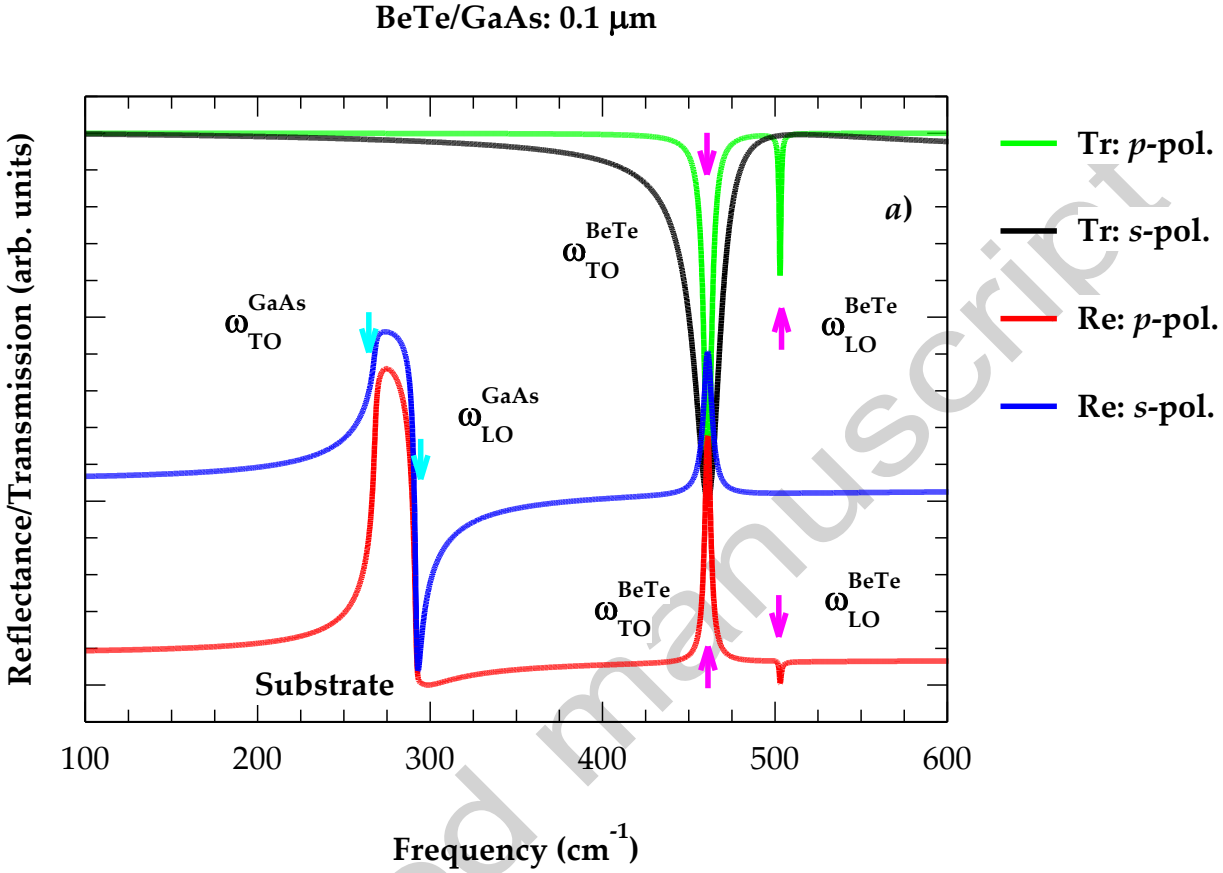

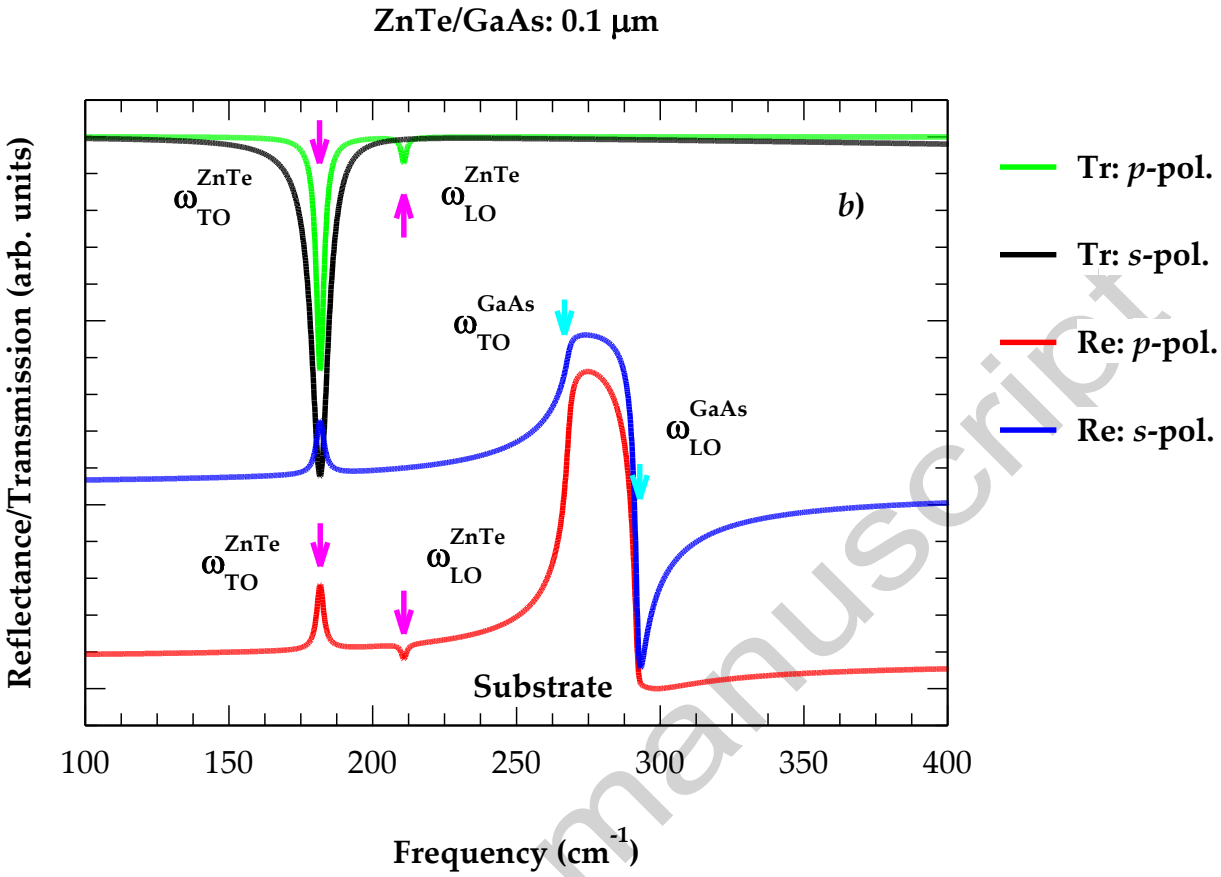

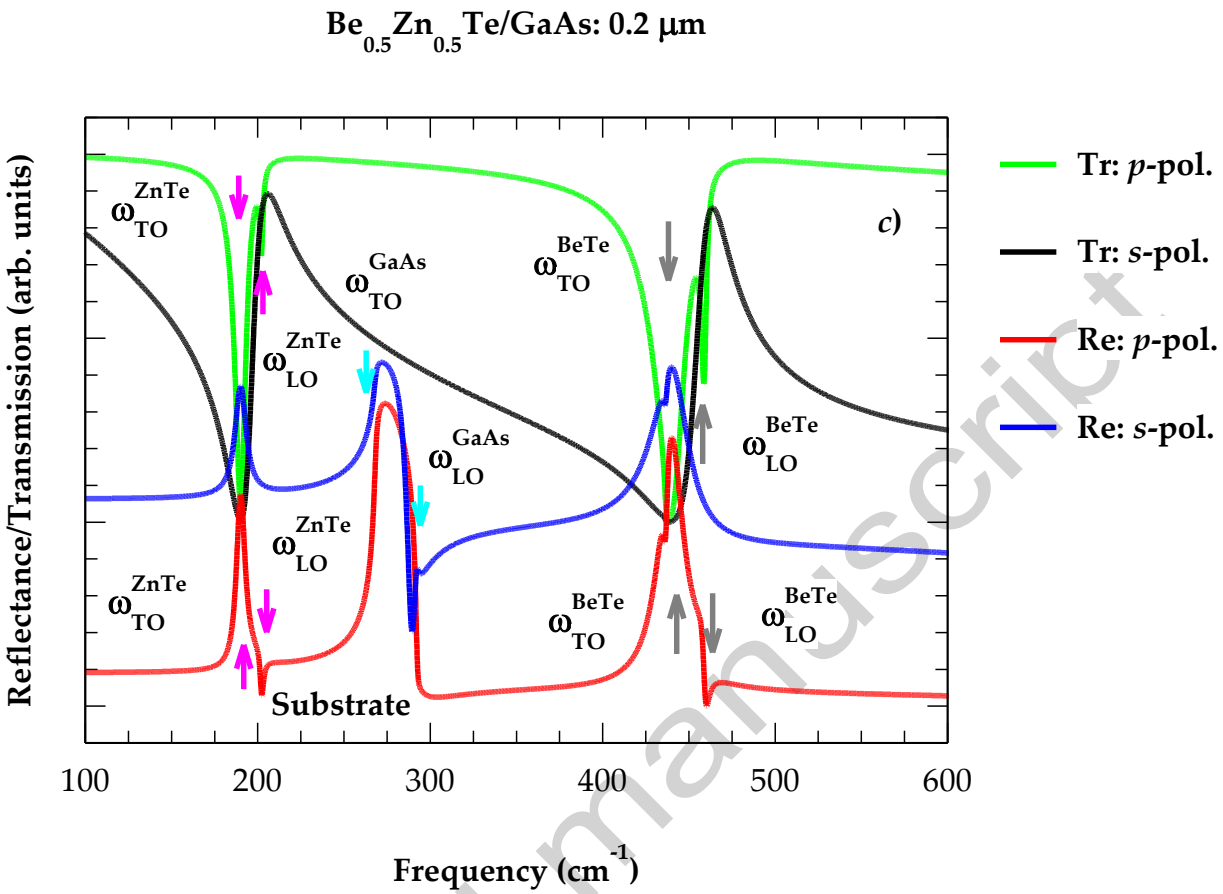

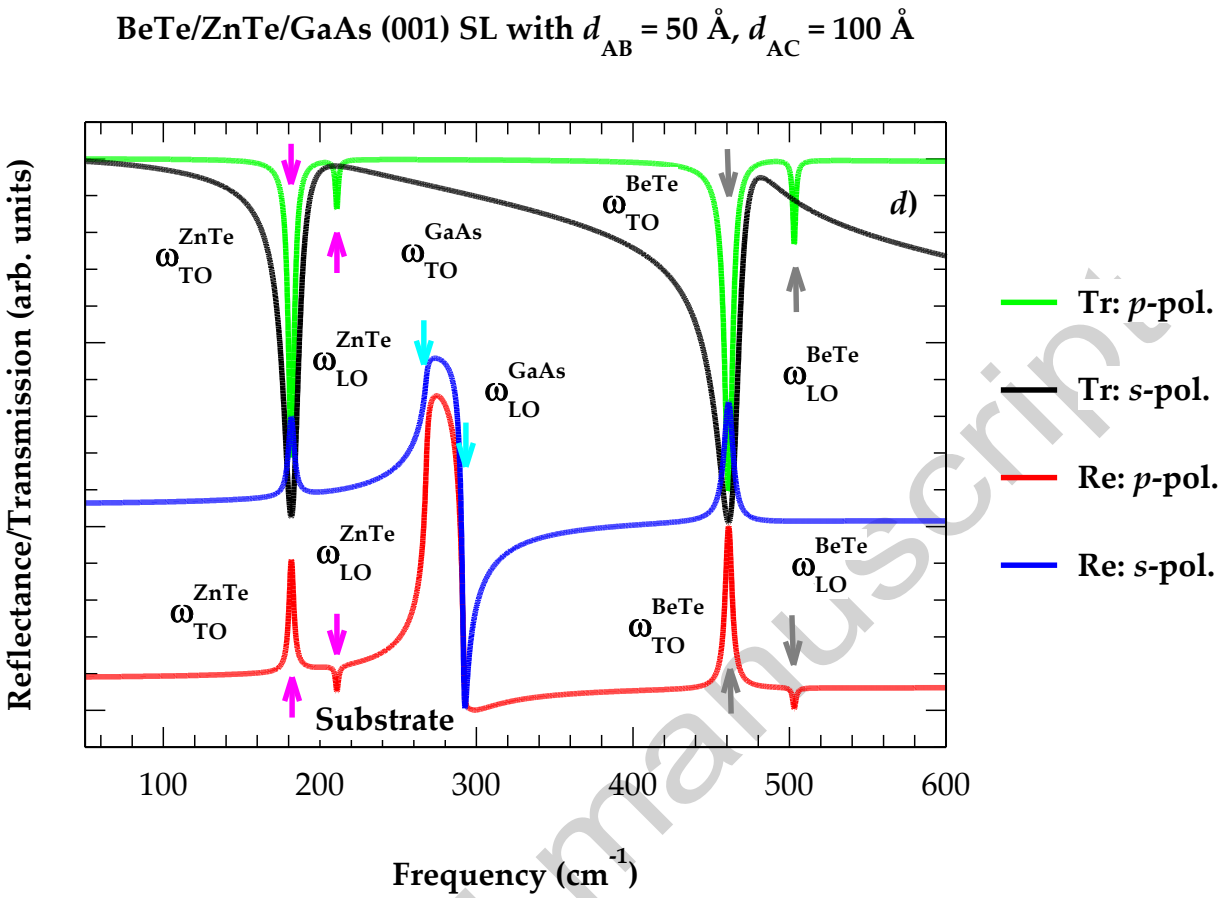

Fig. 2

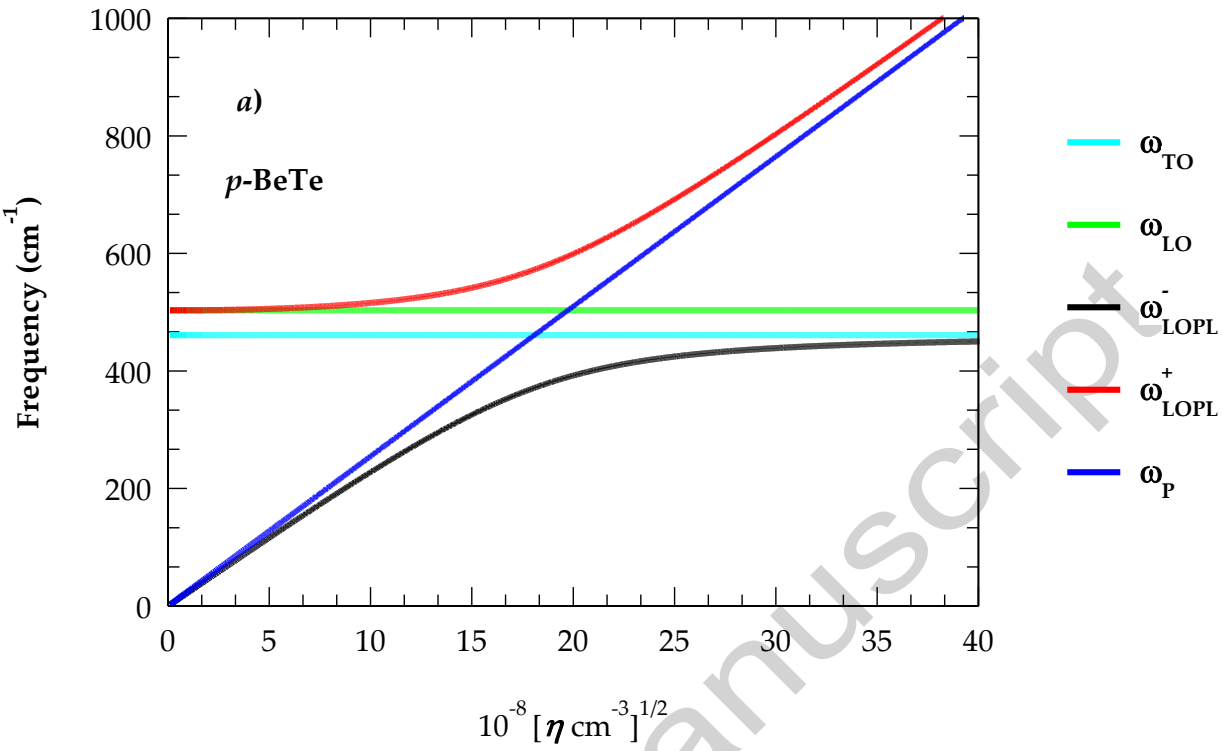

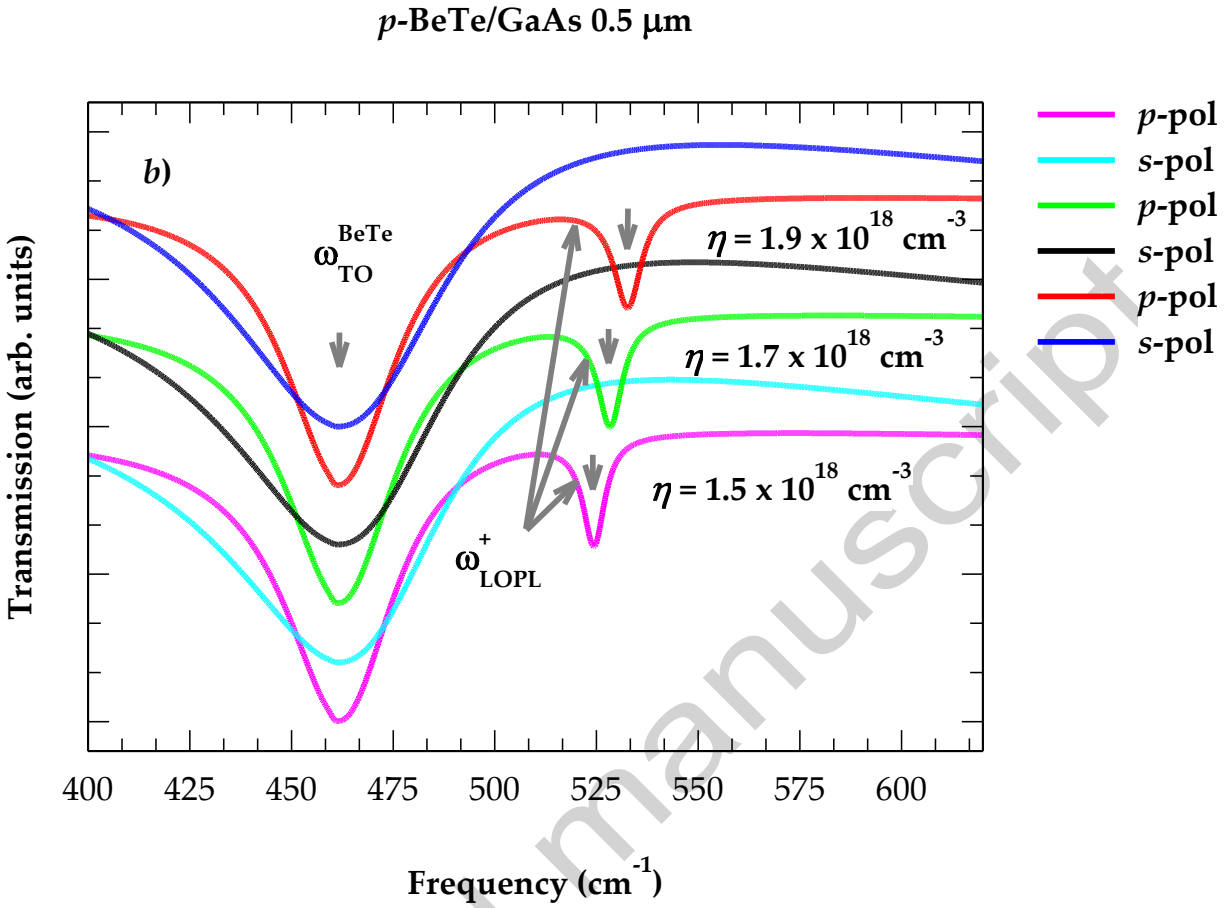

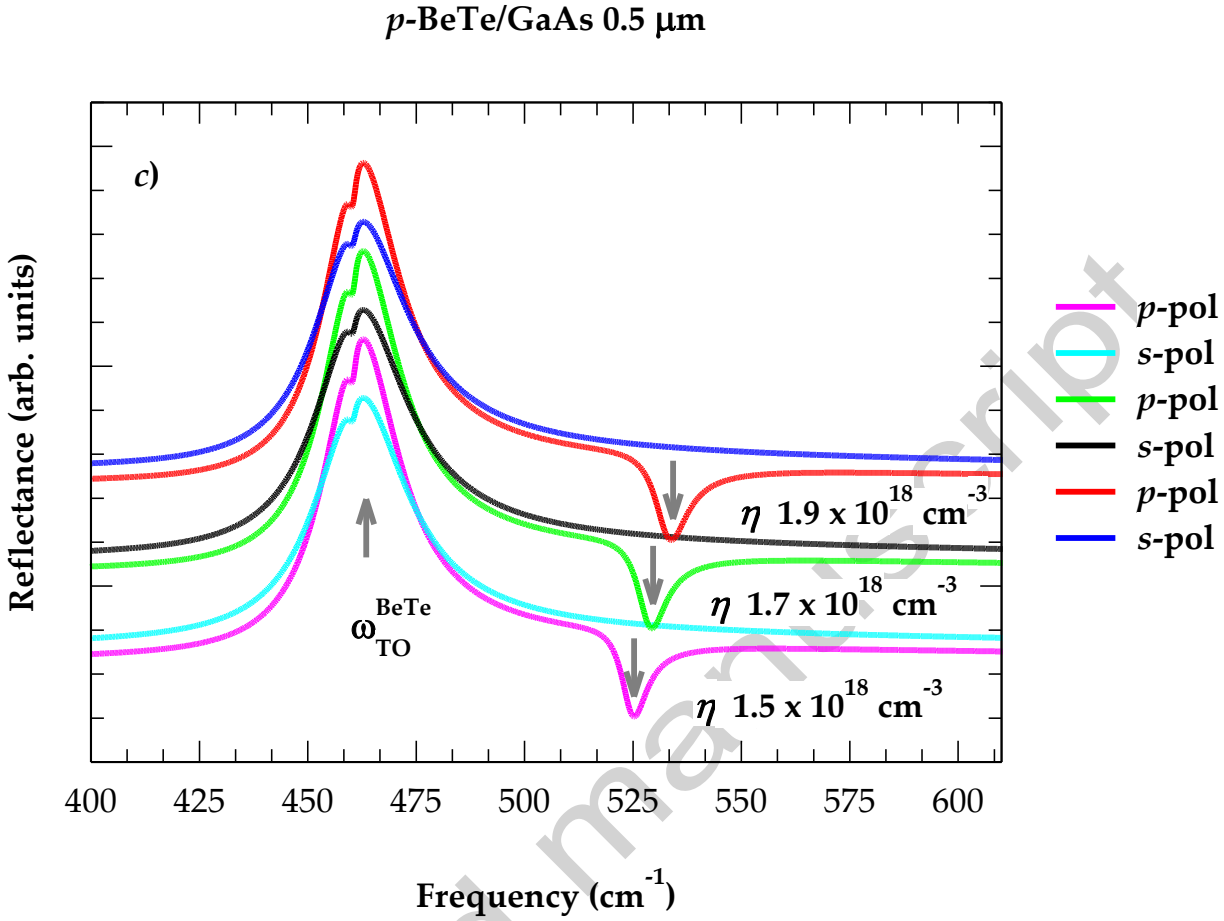

Fig. 3

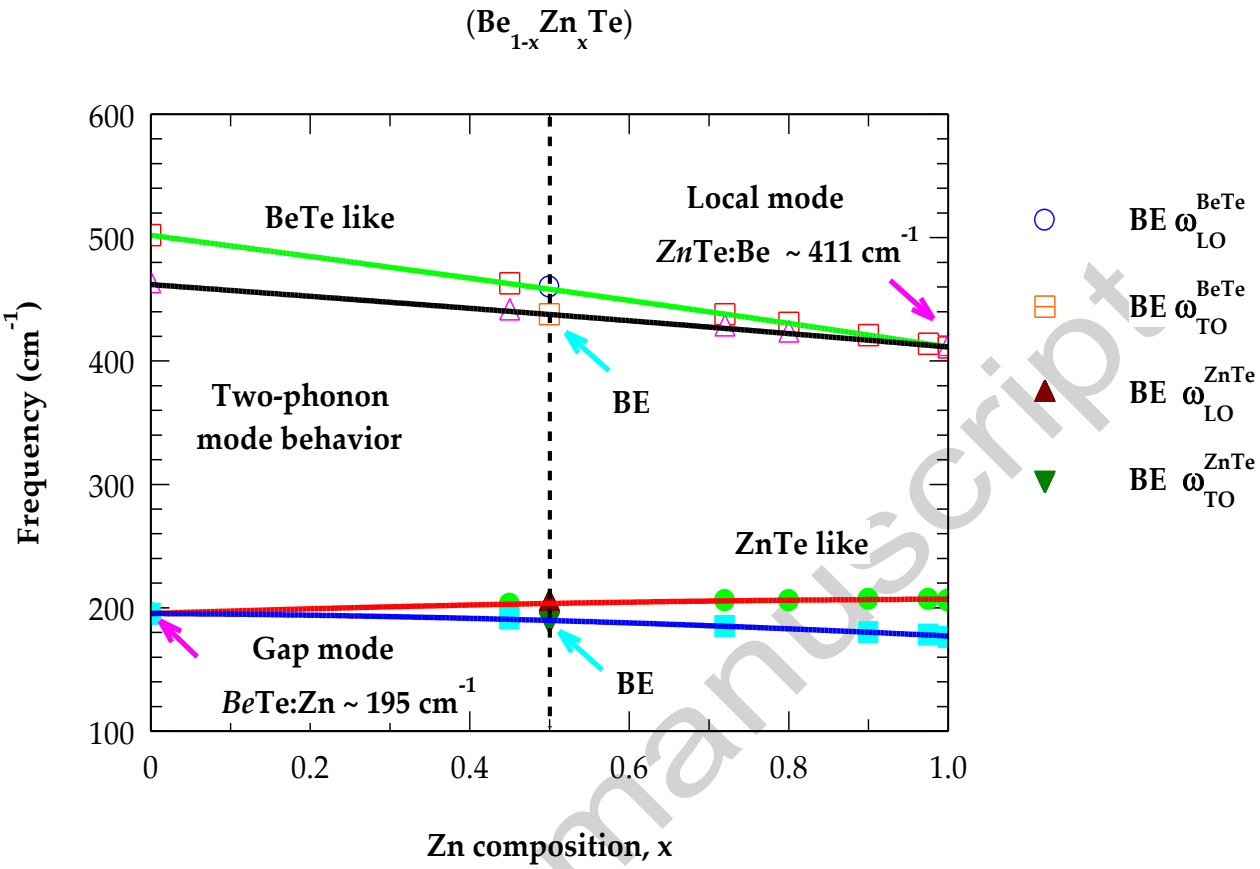

Fig. 4